JACS Au
AN OPEN ACCESS JOURNAL OF THE AMERICAN CHEMICAL SOCIETY

Microneedle-Based DNA Tension Gauge Tethers Enable In Vivo Monitoring of Cell Mechanics during Skin Tissue Regeneration

Xiaofei Ma,[#] Yuanbin Guo,[#] Haotian Li, Chen Zhao, Xuran Dai, Mo Ma, Pinyi Ma, Daqian Song, Yongxi Zhao, Feng Chen,* and Ying Sun*

Cite This: *JACS Au* 2025, 5, 4560−4569

Read Online

ACCESS | Metrics & More | Article Recommendations | Supporting Information

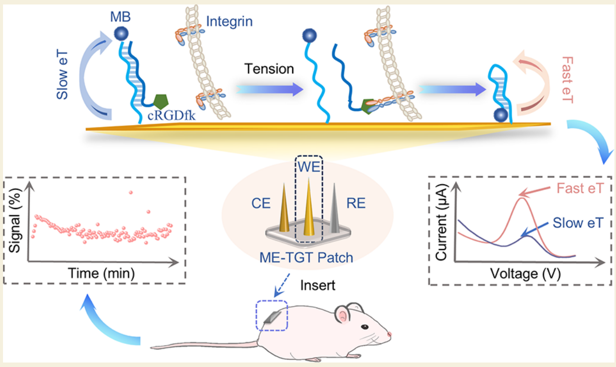

ABSTRACT: The mechanical force exerted by dermal fibroblasts is crucial for promoting cutaneous tissue regeneration and wound healing. However, the implantation of a force interface in vivo or within tissue has become a new challenge in measuring mechanical force. Here, we report a microneedle patch with DNA tension gauge tethers (ME-TGT patch) to monitor the mechanical force of dermal fibroblasts in mice. Microneedles served as the force and electrode interface. When the integrin of the fibroblast membrane is successfully recognized by the integrin ligand (cRGDfk) in the tension probe, the duplex splits irreversibly by cellular mechanical force. The conformation rearrangement driven by a mechanical force can be converted into electrochemical signals. The ME-TGT patch can be used for verification of approximately 12 piconewtons (pN) of mechanical force exerted by fibroblasts in vitro and in vivo. Moreover, we used the ME-TGT patch to monitor cell mechanics during wound healing in skin tissue and found fluctuation (rising first and then falling in the process of 0−14 days) in mice. The ME-TGT patch allowed for monitoring mechanical force on fibroblasts in vivo and provided a novel tool for further research into mechanical mechanisms in tissue regeneration.

KEYWORDS: *Microneedle, DNA tension probes, mechanical force, dermal fibroblasts, tissue regeneration*

INTRODUCTION

Mammalian skin is crucial for protecting organisms from external threats, immune protection, and thermoregulation by sensing external stimulus.[1,2] It comprises three key sections: the epidermis, the dermis, and the skin's vascular network.[3] Dermal fibroblasts play a key role in skin differentiation, tissue homeostasis, and wound healing.[4−6] During skin wound healing, moderate cellular mechanical forces facilitate wound contraction and extracellular matrix (ECM) deposition, whereas abnormal forces (excessive or attenuated) are associated with pathological scar formation and delayed healing.[7−9] Notably, in second-degree scalds, the dynamic changes in fibroblast mechanical force are closely linked to the wound healing process.[10] Therefore, the study of the mechanical force exerted by the dermal fibroblast epidermis is of great significance for promoting tissue regeneration and healing, revealing the mechanical mechanism, promoting the development of tissue engineering, and guiding drug research.

Mechanical forces released by cells refer to the interaction between a cell and its adjacent cells or the surrounding extracellular matrix.[11−14] This mechanical force interaction makes a crucial contribution to regulating a variety of cellular behavior processes, including cell migration, morphological change, and aggressiveness.[15,16] It also plays an important role in cell function and tissue morphogenesis. As transmembrane proteins, the integrin family is one of the main force transduction receptors in cells.[17,18] These receptors mediate force transmission between the ECM and cytoskeleton.[19] They can mediate and transfer mechanical forces between the cell and its microenvironment, which includes the extracellular matrix and neighboring cells. Extensive research efforts have aimed to explore the mechanical forces between cells and the extracellular matrix, such as traction microscopy,[20,21] collagen gels,[22] tissue columns, and microcolumns.[23] Yet, these methods are limited to millimeter and nanonewton scales for length and force, thus hindering molecular-level (piconewton) force transfer research. Salaita's team developed a DNA tension probe. When cells convey molecular forces via a membrane receptor,[24] the probe activates fluorescent signals. In addition, a method called DNA-based tension gauge tether (TGT), developed by Ha's team, was initially designed to

Received: July 14, 2025
Revised: August 21, 2025
Accepted: August 21, 2025
Published: August 28, 2025

Scheme 1. Schematic Diagram of the ME-TGT Patch for Monitoring Mechanical Force In Vivo[a]

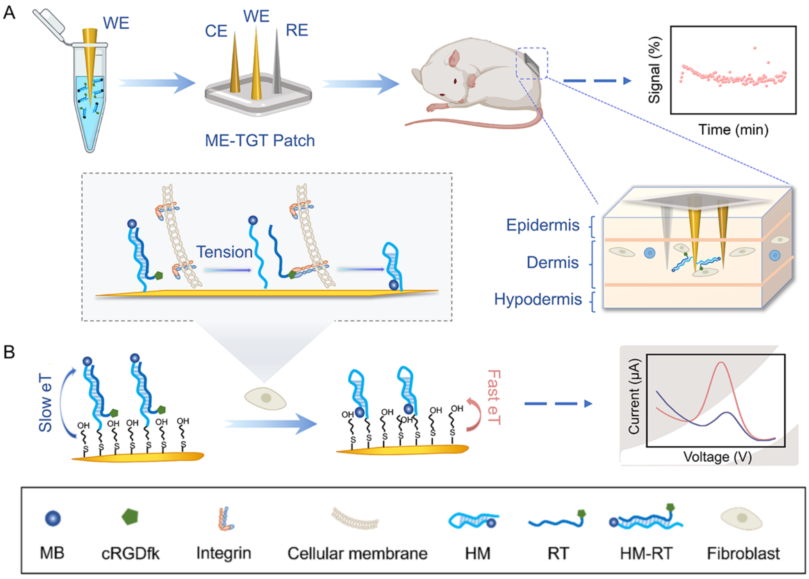

[a](A) Construction procedure of the ME-TGT patch and in situ measurement of dermal fibroblasts. (B) Conformational change mechanism triggered by mechanical force on target cells into electrochemical signals.

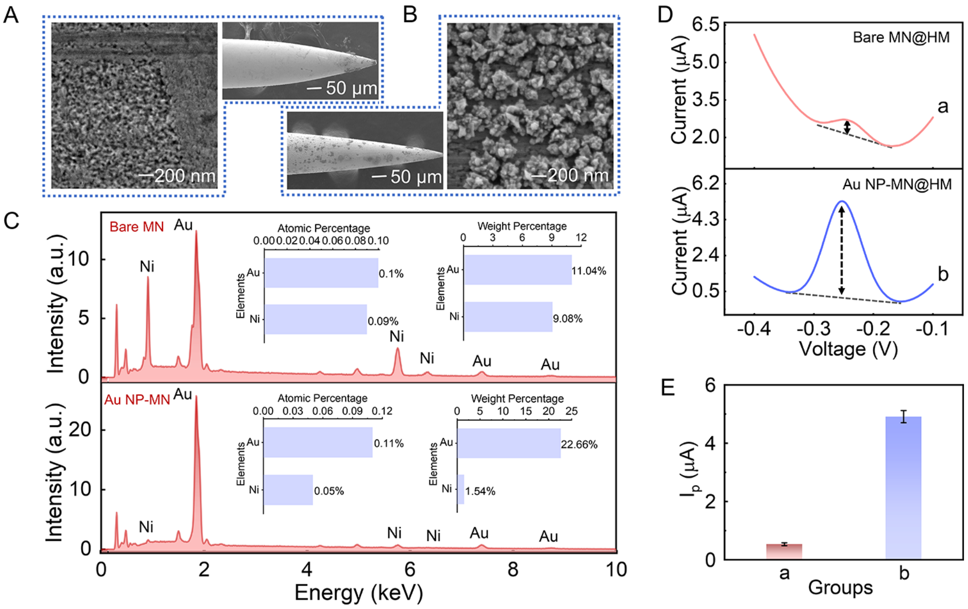

Figure 1. Characterization of Au NP deposition on MNs. (A) SEM image of a bare MN (the tip of the needle is about 4 mm). Scale bar: 50 μm and 200 nm. (B) SEM image of Au NP−MNs. Scale bar: 50 μm and 200 nm. (C) Mapped results further complemented with EDX analysis, showing the elemental composition with atomic and weight percentages. (D) Before and after Au NP deposition, the square-wave voltammetry (SWV) curve of HM-modified MNs. (E) Vector diagram of (D) (mean ± SD, *n* = 3).

regulate the forces exerted by cells and was later extended to record the history of cellular forces.[25] In the above methods, the mechanical force data from cells are chiefly obtained via substrate deformation degrees or fluorescence signal alterations.[26,27] To attain in vitro detection of the mechanical forces exerted by cell release, force interfaces like collagen gel, microcolumns, glass coverslips, and silicon spheres are employed.[28] Nevertheless, these force interfaces cannot be implanted into the body or tissue, which limits in vivo measurement of mechanical force in biological processes such as tissue regeneration.

The microneedles (MNs) can serve as an effective force interface in vivo.[29,30] They are less than 1000 μm in length, are sharp, and are mechanically robust. With their sharp microstructure, MNs can penetrate the stratum corneum of the skin into the interstitial fluid in the dermis without causing pain.[30−32] The previously modified MN devices can minimally invasively monitor cellular or molecular data in skin interstitial fluid.[33,34] Their penetration depth is shallow (∼1 mm), so they neither reach nerve endings nor penetrate the dermal vasculature. Consequently, MNs can directly access the interstitial fluid and painlessly contact fibroblasts. MNs have been previously shown, mainly for drug delivery[35] or in vivo

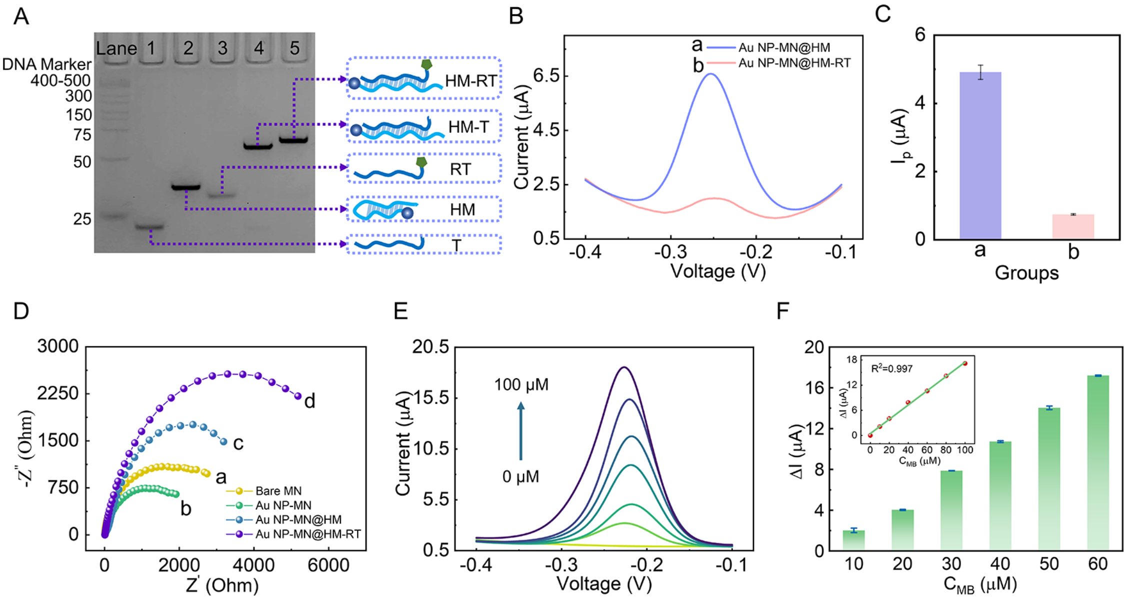

Figure 2. Characterization and electrochemical analysis of DNA assembly and modified microelectrodes. (A) PAGE analysis of RT and HM-RT assembly of ME-TGT (concentration of DNA strands:1 μM). (B) SWV signals of Au NP-MN@HM and Au NP-MN@HM-RT in 10 mM PBS solution. (C) Vector diagram of (B) (mean ± SD, $n = 3$). (D) Electrochemical impedance spectroscopy (EIS) of different microelectrodes with different modifications in a conventional potassium ferricyanide (5 mM) solution. (E) Determination of predeposited MNs in different concentrations of MB solutions. The concentrations are 0, 10, 20, 40, 60, 80, and 100 μM in sequence. (F) Vector diagram of (E), (mean ± SD, $n = 3$). The illustration on the top left shows a linear correlation curve based on the concentration of MB vs current intensity.

affinity detection.[36] Hence, it is ideal to engage the MNs as a force interface in vivo to explore such mechanical force in dermal fibroblasts.

In this study, we developed a ME-TGT patch for exploring the piconewton forces exerted by fibroblast-surface receptors within the living skin dermis (Scheme 1). In the ME-TGT patch, microneedles served as the force and microelectrode interface. The TGT probe (also named HM-RT) mainly comprises HM and RT. HM refers to the hairpin chain (H) modifying methylene blue (MB), and RT refers to the toehold chain (T) modifying cRGDfk in this paper. Initially, the TGT probes are anchored on the microelectrode surface through the Au−S bond.[37,38] When the probes contact the target cells, the cRGDfk couples with integrins on the membrane, resulting in mechanically tension-driven conformational rearrangement of hairpin chain molecules (Scheme 1B). This method enables real-time conversion of weak cell mechanical force-triggered signals into electrochemical signals. In this way, the mechanical force of living dermal fibroblasts can be monitored in vivo (Scheme 1A). By combining the high electrochemical sensitivity with the skin-penetrating function of MNs, the ME-TGT patch can expand the pool of detectable analytes with mechanical force in vivo.

■ RESULTS AND DISCUSSION

Au NP Deposition on MNs via Cyclic Voltammetry for TGT Probe Anchoring

We opted for a classic strategy of depositing the microneedle surfaces with thiol-affinity substances for TGT probes anchoring to MNs.[39] The local electrochemical reduction of gold ions guarantees that Au NPs adhere to the microneedle electrode surface tightly and firmly.[40,41] Moreover, this modification can also alter the surface properties and chemical reactivity of MNs, enabling them to bind more TGT probes. Consequently, we chose cyclic voltammetry to deposit Au NPs on the microelectrode surface tightly and firmly, thus laying a solid foundation for TGT probe modification and subsequent applications.

Initially, field emission scanning electron microscopy (SEM) and energy-dispersion spectroscopy (EDS) were used to represent the surface morphologies of MNs before and after Au NP deposition. Figure 1A presents the surface morphology of bare MNs without Au NP deposition, revealing a relatively smooth and homogeneous microstructure. At the same time, Figure 1C (along with Figure S2) shows the composition and distribution of its characteristic elements, namely, Au, Ni, and others. After the deposition of Au NPs on the MNs, the morphology of the Au NPs adhered to them is depicted in Figure 1B. These nanoparticles appear as nonuniform spherical particles, approximately 100 nm in diameter, with favorable monodispersity. Several raised particles were present at the microneedle interface. Although aggregations occur, they provide more binding sites for probe modification. Eliminating nickel exposure is crucial since nickel and its surface oxide layer can impede the modification of TGT probes during signal retrieval. Comparing the elemental composition and distribution in Figure 1C, the result showed a significant attenuation of nickel-related peaks. The atomic percentage of nickel decreased from 0.09 to 0.05%, and the mass percentage decreased from 9.08 to 1.54%. Conversely, the atomic percentage of gold remained at 0.11%, and its mass percentage increased markedly from 11.04 to 22.66%. The weight of Au atoms is 1.1 times that of the undeposited microneedle interface.

To further validate the deposition efficiency, a simplified model was initially constructed at the interface of two MN types. Voltammetric measurements in PBS were conducted using the interfacial electrochemical signaling of MB. As shown in Figure 1D,E, the reduction peak of MB was distinct on Au NP-deposited MNs. In contrast, on the bare MNs, the

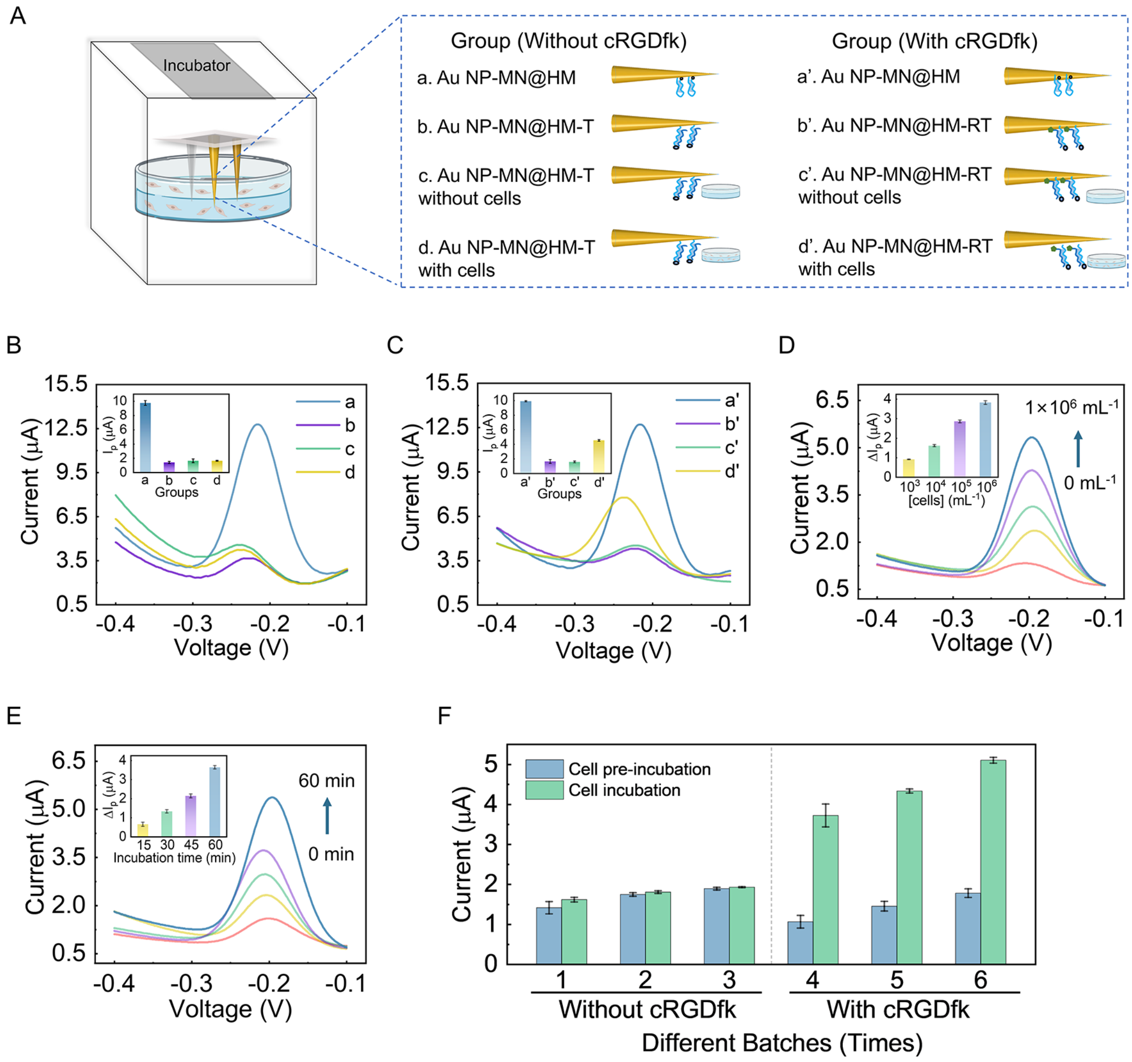

Figure 3. Detection of cellular mechanical forces using the ME-TGT patch in vitro. (A) Schematic diagram of the cell mechanical force test in vitro. (B) SWV signal without cRGDfk on the T-chain and the vector diagram of (B) (mean ± SD, $n = 3$). (C) SWV signal with cRGDfk on the T-chain and the vector diagram of (C) (mean ± SD, $n = 3$). (D) SWV responses of the ME-TGT patch with different concentrations of cells (the incubation concentrations were 0, 10^3, 10^4, 10^5, and 10^6 fibroblasts/mL in sequence.) (E) SWV responses of the ME-TGT patch with different incubation times in 1×10^6 fibroblasts/mL (the incubation times were 0, 15, 30, 45, and 60 min in sequence). (F) Changes of current of different batches before and after cell incubation (mean ± SD, $n = 3$).

reduction peak of MB was nearly indistinguishable from the background noise. These data indicated that the MNs deposited with Au NPs increase the specific surface area, providing more binding sites to anchor the TGT probes. Meanwhile, the gold layer can increase the friction coefficient and the specific surface area under specific conditions. These factors are crucial for the ME-TGT patch to boost the signal-to-noise ratio, accuracy, and other sensing capabilities.

Design and Characterization of the ME-TGT Probe for Cellular Force Measurement

Polyacrylamide gel electrophoresis (PAGE) was employed to investigate the time-dependent binding of cRGDfk-DBCO and Toehold-N_3 (the process diagram is presented in Figure S3). We compared the assembly efficacy across four different assembly time intervals (Figure S4). Notably, assembly yield was nearly constant after 1 h. The ME-TGT probe (NUPACK-derived theoretical simulation results of the TGT probe are presented in Figure S5), constructed to exhibit structural homology with previously developed TGT probes, underwent cleavage at ∼12 pN under the influence of cellular forces.[25,28] While there were differences in the ligand modification mode and force direction, the assembly process of cRGDfk with T, HM with T, and HM with RT was characterized by PAGE in an enzyme-free buffer containing Mg^{2+}. The fabrication of the TGT probe and MS analysis of intermediates are shown in Figures S3, S6, and S7. In Figure 2A, lanes 1 to 5, in turn, represent T, HM, RT, HM-T, and HM-RT. Lane 5 exhibited the lowest mobility, demonstrating successful assembly of HM and RT. The shift between lanes 3 and 1 indicated that cRGDfk and Toehold bound successfully via click reaction.

Subsequently, we resorted to electrochemical voltammetry to authenticate the successful anchoring of HM-RT onto the MNs. The ME-TGT probe comprised two DNA strands. Precisely, the distal extremity (specifically, the 5′-terminus) of the HM strand was tagged with MB. Single-nucleotide redox potential is usually out of the electrochemical window, so redox units, such as MB, are linked to the DNA strand end to facilitate charge injection for studying solution-state DNA charge transfer.[42] As depicted in Figure 2B,C, merely the microneedle electrode modified with HM manifested robust and prominent current signals, while current signals were significantly attenuated on the HM-RT-modified microneedle electrode. The electrochemical signal strength of the former MB (4.822×10^{-6}) was 7.61 times that of the latter (6.340×10^{-7}). This is because, in the same sensing environment, the two modifications present different conformations. Upon adhesion with the target cell, irreversible conformational alterations will be induced due to the presence of cellular mechanical forces. These alterations, in turn, trigger variations in the redox current between the molecule and the electrode, as reported by the electrochemical signal.[43,44] Such changes with mechanical forces can be gauged via square-wave voltammetry.

It has been proven that electrochemical impedance spectroscopy (EIS) is an effective characterization method to confirm the successful construction of biosensors.[45] The Nyquist diagram of the stepwise modification of the microneedle electrode was recorded in the conventional potassium ferricyanide (5 mM) solution. As shown in Figure 2D, the impedance values of the bare microneedle electrode are lower (curve *a*). After the deposition of Au NPs, the impedance value of the electrode is significantly reduced (curve *b*). The reason for this is that the gold layer enhances the conductivity of the microelectrodes, thereby reducing their impedance. Simultaneously, the flatness promotes charge distribution, enhancing the reaction efficiency and electrical conductivity. Subsequently, further modification of HM and RT onto the deposited gold microelectrode led to a significant increase in impedance values (curves *c* and *d*). This is attributed to the mutual repulsion between the negatively charged DNA and $[Fe\ (CN)_6]^{4-/3-}$ in the solution, which impedes charge transfer and thereby increases the impedance value.[46] These results fully confirm the successful construction of the ME-TGT probe.

To confirm the anchoring of the beacon molecule MB onto the microneedle electrode surface and the influence of Au NP deposition on the response signal, we gauged the square-wave responses of freely diffusing MB molecules at diverse concentrations. As depicted in Figures 2E,F, and S8, the MNs were solely deposited with 1-hexyl mercaptan. For both bare and Au-deposited MNs, free MB showed relatively stable peak potentials and excellent linearity, with R^2 values of 0.997 and 0.998, respectively. The results suggest that the change in the electrode surface does not significantly alter the electrochemical activity of MB.

Integrin-Specific ME-TGT Patch for Monitoring Cellular Mechanical Forces In Vitro

Integrin $\alpha v\beta 3$ expressed on the surface of the cell membrane mainly recognizes ligands in the ECM via specific structural regions. It can highly specifically identify the above-mentioned cRGDfk on the ME-TGT patch and effectively promote the occurrence of force-mediated cell mechanical force. They are much like a specific key (integrin $\alpha v\beta 3$) fitting a particular lock (cRGDfk), triggering an electrochemical signal.

To investigate the cytotoxicity of ME-TGT patches, we employed the CCK8 assay to evaluate the cytotoxicity of various microneedle electrodes against live cells in vitro before carrying out the mechanical force measurement. This was to ensure that ME-TGT patches had no adverse effects on cellular health in further investigations (Figure S11). Cells incubated with 10 or 100 μL of CCK8 for 24 h showed viability exceeding 80%. The results demonstrated that the microneedle interface does not undermine cellular health and validated its applicability in subsequent living cell experiments.

Subsequently, multiple control experiments were set up to investigate the current change during adhesion of the fibroblast integrins and the cRGDfk with RT triggers. Here, the samples are divided into two groups, one group without cRGDfk (a, b, c, and d) and the other group with cRGDfk (a', b', c', and d'), as shown in Figure 3A. When the microneedle electrodes were cultured in the areas with cells (400 μL 1×10^6 fibroblasts/mL) and without cells for 60 min, the peak current showed almost no change in the absence of cRGDfk (curves *c* and *d* in Figure 3B). This indicated that the T-chain without cRGDfk cannot measure the mechanical force of the cells. The peak current was enhanced significantly in the presence of both cRGDfk and target cells (curve *d* in Figure 3C), demonstrating that the T-chain with cRGDfk possesses the ability to detect cellular mechanical force. The augmented square-wave voltammetry current verified the reduction of the RT initiation chain on the microneedle electrode surface. Since RT was released upon culturing the microneedle with target cells, the interfacial conformation of TGT probes changed. The experimental results showed that dissociation of the T-chain does not occur without the interaction mediated by cRGDfk, and the mechanical force of cells does not affect the sensing signal under these circumstances.

Subsequently, to further study the sensitivity of the ME-TGT patch to mechanical forces from cells in vitro, we performed concentration-dependent and time-dependent tests on target cells. As shown in Figure 3D, the ME-TGT patch was incubated in cell gradients of about 0, 1×10^3, 1×10^4, 1×10^5, and 1×10^6 fibroblasts/mL for 60 min. As the cell concentration gradually increased, the peak current increased markedly. The probable reason is that more cells enable HM-RT at the microneedle interface to release the RT chain more thoroughly. It enables efficient charge conduction between MBs and the microneedle electrode interface.

Additionally, at a cell density of 1×10^6 fibroblasts/mL, incubation was carried out at 0, 15, 30, 45, and 60 min. The peak square-wave voltammetric current of MB increased remarkably with the incubation time (Figure 3E). Presumably, a longer incubation duration facilitates the contact between target cells and the initiating probes at the microneedle interface, thus increasing the current signal. Additionally, to assess the reproducibility and batch-to-batch consistency of ME-TGT patches, signal intensity variations of surface-modified MNs from distinct batches were characterized before and after incubation with cells. As shown in Figure 3F, the peak current of the electrodes within the same batch remained relatively unchanged before and after cell incubation. For electrodes from different batches, the peak current was almost constant. The properties of the patch exhibit good batch-to-batch stability, thus enhancing the reliability and repeatability of ME-TGT patches.

In Vivo Exploring Cellular Mechanical Force by the ME-TGT Patch during Wound Healing

This section further focuses on whether the patches can achieve the in vivo detection of mechanical forces. In vivo detection allows cellular mechanical forces to be observed and measured in their native physiological state. It is effective in preventing changes in the cell state caused by sample manipulation and other procedures. Here, the relative peak

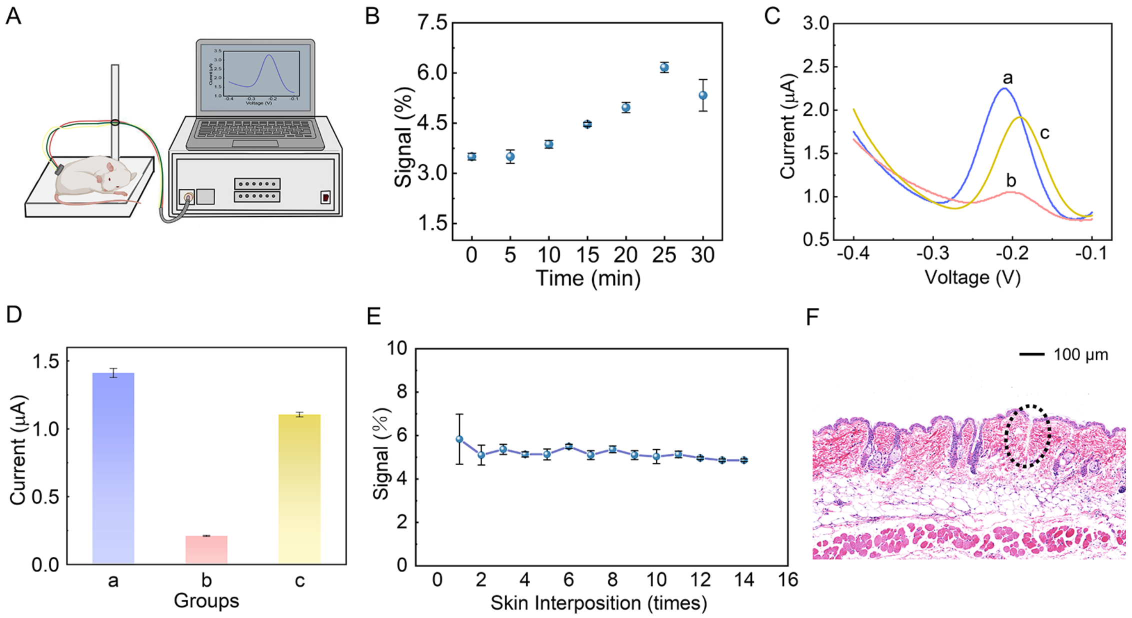

Figure 4. Monitoring of cellular mechanical forces in living mice using the ME-TGT patch. (A) Schematic diagram of the ME-TGT patch for the measurement of mechanical forces in living mice. (B) SWV signal response of patches at different times (mean ± SD, $n = 3$). (C) Voltammograms of the patches under the optimal incubation time of mice in Figure 4B. (a) Au NP-MN@HM with dermal fibroblasts for 25 min. (b) Au NP-MN@HM-RT with dermal fibroblasts for 0 min. (c) Au NP-MN@HM-RT with dermal fibroblasts for 25 min. (D) Vector diagram of (C) (mean ± SD, $n = 3$). (E) Signal response of the insertion experiment (mean ± SD, $n = 3$). (F) Skin permeability test in mice. Scale bar: 100 μm.

current change was used to represent the signal response to minimize interdevice variations.[44] As shown in Figure 4B, it detected cellular mechanical force properties within the skin interstitial fluid and probed their correlation with time variables. Three healthy mice were selected as experimental subjects in the above experiment. During the experimental operation, the preprepared ME-TGT patch was accurately attached to the lower back area of anesthetized mice where hair had been removed and properly anchored with medical tape (Figure 4A). Based on this, the electrochemical signal response (detailed theoretical calculations are presented in the SI) was monitored for 30 min. The results indicated that the signal response reached its optimum at 25 min and then started to decline (Figure 4B). An overly long duration of in situ detection is highly prone to cause partial degradation or loss of the ME-TGT due to the distinctive in situ physiological environment, which will adversely affect the signal response. Subsequently, within the optimal 25 min time frame determined previously, the MNs were incubated with living cells, using unincubated microneedles (modified probes) as a blank control. After incubation for 25 min (Figure 4C), the peak current increased to 5.40 times. This fully affirmed that conformational changes induced MB close to the electrode surface, strongly suggesting the existence of mechanical forces between dermal fibroblasts and the external environment of the interstitial fluid.

The selectivity of the ME-TGT patch was evaluated in the presence of common electroactive ISF components and potential interferers (Figure S12), including ascorbic acid (AA, 5 mM), uric acid (UA, 5 mM), acetaminophen (AP, 5 mM), K^+ (10 mM), Na^+ (10 mM), Mg^{2+} (10 mM), glucose (Glu, 5 mM), and lactic acid (Lac, 5 mM). Square-wave voltammetry was used to test the patch against 400 μL of the target analyte solution (1×10^6 fibroblasts/ml). The result had shown that the ME-TGT patch exhibited high selectivity toward target fibroblasts and notable anti-interference capability, laying a solid foundation for subsequent in vivo mouse tests.

To test the long-term stability of the probe in the cell culture medium, we investigated the stability of a 4 μM DNA probe in 10% serum for 48 h. As indicated by PAGE, the degradation rate of the DNA probe was ≤5% within the initial 2 h, whereas it exceeded 60% after 8 h treatment (Figure S13). Therefore, the probe cannot be tested for a long time in vivo. However, during wound healing, different batches of the same-structured probes were used to avoid probe degradation in long-term detection. The ME-TGT patch exhibited excellent batch-to-batch stability (Figure S14), enabling the subsequent scald experiment to be conducted for up to 14 days. This result ensured the effectiveness of microneedles with different batches in testing different healing stages after scalds.

As shown in Figure S15, to investigate the antidegradation ability of the probe in the mice, we first modified cRGDfk-free TGT probes (HM-T) onto microneedles (working microelectrodes). After subcutaneous insertion in mice, we tested the signal duration and found that it remained stable within 120 min, providing a solid foundation for subsequent research. Meanwhile, the signal duration of the cRGDfk-modified TGT probe (HM-RT) in mice dermis was investigated. The electrochemical signal response peaked at 25 min and then gradually decayed with time. This may be attributed to proteolytic degradation of cRGDfk, which hindered cell adhesion or cellular force.

The stability of ME-TGT patches is critical for accurate monitoring of the cellular mechanical force in vivo. Therefore, this section aimed to assess the impact of skin insertion disruption on the performance of patches, verifying the insertion stability of ME-TGT patches in vivo. Following insertion of the ME-TGT patch into mouse skin and 25 min incubation, responses of dermal fibroblasts to its repeated dorsal insertion were measured and compared. Signal collection intervals were ~30 s. As presented in Figure 4E,

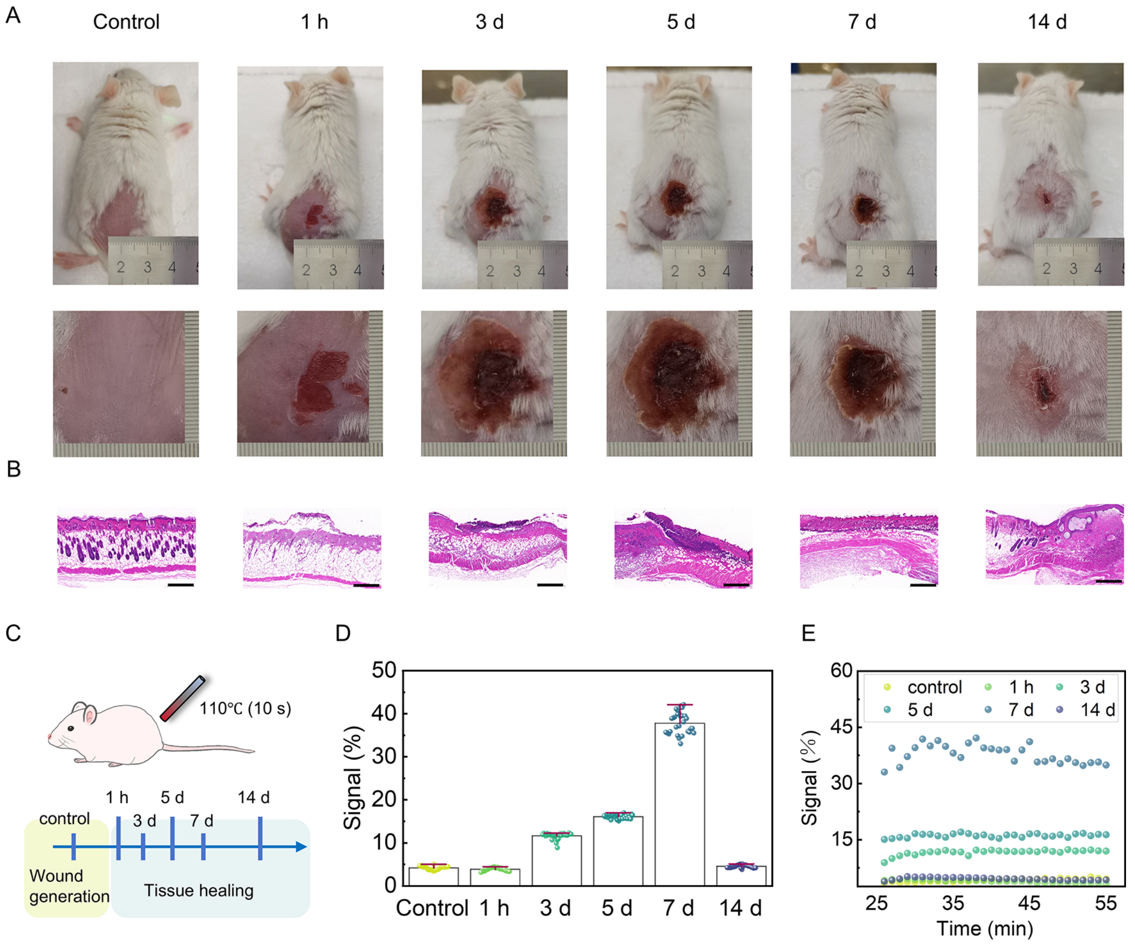

Figure 5. Monitoring wound healing progression in scalded mice using the ME-TGT patch through electrochemical signals and histological analysis. (A) Images and local magnifications of wounds at different times; units are in mm. (B) H&E staining of the wound tissue at different times. Scale bar: 500 μm. (C) Schematic diagram of the scalding experiment in mice. (D) SWV signal response of the patches under different healing periods of the scald wound. (E) Scatter plot of signal response during postscald healing at different healing periods after 25 min of incubation. Follow-up time point: hour (h); day (d).

the signal response of the ME-TGT patch fluctuates within the 5−6% range, with a fluctuation rate below 10%, indicating a relatively stable trend of signal variation. This result confirmed the excellent robustness of the microneedle tension-sensing layer when faced with insertion disruptions. Moreover, it offers assurance that ME-TGT can carry out detection tasks in a complex in situ environment.

Subsequently, to more effectively attain a signal response to mechanical forces exerted by viable dermal fibroblasts, comprehensive evaluations were conducted on the tissue permeability and skin biocompatibility of the microneedle segment in ME-TGT. After the insertion of ME-TGT patches, the rat skin tissue stained with Hematoxylin and Eosin (H&E) was presented (Figure 4F), which verified that the developed microneedle device had pierced the epidermis and infiltrated the dermal layer of the skin (Figure S16). Meanwhile, upon patch removal, no obvious bleeding was observed on the skin wound (Figure S17), and the wound quickly recovered in a short time. This fully demonstrated the noninvasive or minimally invasive characteristics of the detection method for living organisms in this study.

Microneedle insertion exerts localized, transient effects on contacted cells due to inherent physical and potential chemical factors. Physically, the medical-grade (30 gauge) lancets and acupuncture needles possess high mechanical strength, biocompatibility, slender and sharp tips, and smooth surfaces, minimizing insertion force and tissue damage compared to thicker or barbed alternatives.[47,48] Insertion depth was precisely controlled to target the dermal layer, reducing compression damage, and needles were inserted slowly and smoothly to avoid shear forces and tearing. Chemically, the Au nanoparticle and nucleic acid functionalization on the working electrode surface has minimal unintended cytotoxicity, supported by extensive biocompatibility evidence and low cytotoxicity demonstrated in Figure S11 for all electrodes.[49] Furthermore, ultraviolet (UV) disinfection and autoclaving preuse minimize bacterial contamination. Importantly, the anisotropic, viscoelastic nature of skin tissue causes bending during insertion, affecting depth measurement accuracy and making some localized cell damage inevitable.[50,51]

Next, we used a scald wound healing mouse model to validate fibroblast mechanical forces at different stages of skin tissue regeneration. The patches were applied to the wound site and incubated for 25 min prior to electrochemical testing at sequential healing stages. The scalded mice were divided into six groups based on postscald observation time points: the control groups (I: natural growth) and the experimental group (II: 1 h after the scald, III: 3 days after the scald, IV: 5 days after the scald, V: 7 days after the scald, VI: 14 days after the scald). The status of the scald wounds was observed and recorded on 1 h and 3 d, 5, 7, and 14 d. As presented in Figure 5A, wound areas in mice demonstrated a significant reduction over the 14-d healing period. H&E staining of skin tissues revealed marked histological differences between experimental and control groups through histopathological analysis. Inflammatory cell infiltration with disorganized dermal architecture was revealed by H&E staining at 3 d, which transitioned to mild inflammatory infiltration accompanied by fibrous tissue proliferation at 14 d (Figure 5B). Scald wound healing stage morphologies were closely correlated with the electrochemical signal response, as presented in Figure 5D,E. Electrochemical signal response in the control group remained stable at ∼5%, indicating stationary adhesion states of normal dermal fibroblasts with weak interference. At 1 h postscald, the electrochemical signal response remained at 4% with no significant fluctuations. Fibroblasts displayed direct thermal injury characterized by partial necrosis and impaired adhesion. At 3 days postscald, signal response increased to 12%, histologically correlating with fibroblast migration toward the wound interface (Figure 5B). This increase was mechanistically associated with integrin-mediated adhesion forces inducing probe conformational changes via real-time chain traction, thereby accelerating electron transfer. At 5−7 d postscald (signal intensity: 15−40%), rapid signal amplification coincided with fibroblast proliferation and significant probe structural reorganization. At 14 d postscald, decreased fibroblast activity and apoptosis resulted in signal regression to nonscalded levels (signal intensity ∼5%). The above results showed that the electrochemical signal trajectory reflects fibroblast mechanical force during healing.

CONCLUSIONS

Exploring cellular mechanical forces in vivo holds great significance for cutaneous tissue regeneration, wound healing, and guiding drug development. Traditional force interfaces cannot be noninvasively implanted into the skin for cellular mechanical force measurements. To address this limitation, we developed the ME-TGT patch for mechanical force measurement in vivo. Microneedles served as the force and electrode interface. This patch made HM-RT probes immobilized on microelectrode surfaces, which recognize fibroblast integrin via cRGDfk binding, enabling real-time conversion of weak mechanical forces (∼12 pN) into electrochemical signals both in vitro and in vivo. To validate the clinical relevance of this system, we used a scald wound healing mouse model to validate fibroblast mechanical forces at different stages of skin tissue regeneration. The electrochemical signal trajectory reflected the fibroblast mechanical force during healing. Beyond immediate applications, this platform would serve as a novel tool for transmitting mechanical signals at varying tissue depths, enabled by highly programmable DNA-encoded probes of different heights on the MN array.

However, several challenges warrant further exploration. First, the migration mechanism influenced by mechanical force in confined conditions remains unclear, which may form the basis for future research. Second, due to the random insertion of MNs, dermal fibroblasts might evade contact with probes, preventing integrin−cRGDfk interaction and resulting in irregular or absent signals. Additionally, complex in vivo biological mechanisms could generate false positives. These unresolved issues highlight the need for refined probe spatial distribution and signal validation protocols in subsequent studies.

ASSOCIATED CONTENT

Supporting Information

The Supporting Information is available free of charge at https://pubs.acs.org/doi/10.1021/jacsau.5c00870.

> Experiment section, method and theory, basic principles of electrochemical reading, EDS mapping, the schematic diagram of the ME-TGT formation, optimization of RGD-Toehold synthesis, the MS spectrum, pH optimization, cytotoxicity test, selectivity and stability of the patch, permeability and biocompatibility, and bleeding at the skin implantation site in mice (PDF)

AUTHOR INFORMATION

Corresponding Authors

Ying Sun − *College of Chemistry, Jilin Province Research Center for Engineering and Technology of Spectral Analytical Instruments, Jilin University, Changchun 130012, P. R. China;* orcid.org/0000-0002-6820-3184; Email: yingsun@jlu.edu.cn

Feng Chen − *Institute of Analytical Chemistry and Instrument for Life Science, The Key Laboratory of Biomedical Information Engineering of Ministry of Education, School of Life Science and Technology, Xi'an Jiaotong University, Xi'an, Shaanxi 710049, P. R. China;* orcid.org/0000-0003-0188-6256; Email: fengchencf@mail.xjtu.edu.cn

Authors

Xiaofei Ma − *College of Chemistry, Jilin Province Research Center for Engineering and Technology of Spectral Analytical Instruments, Jilin University, Changchun 130012, P. R. China*

Yuanbin Guo − *Institute of Analytical Chemistry and Instrument for Life Science, The Key Laboratory of Biomedical Information Engineering of Ministry of Education, School of Life Science and Technology, Xi'an Jiaotong University, Xi'an, Shaanxi 710049, P. R. China*

Haotian Li − *Institute of Analytical Chemistry and Instrument for Life Science, The Key Laboratory of Biomedical Information Engineering of Ministry of Education, School of Life Science and Technology, Xi'an Jiaotong University, Xi'an, Shaanxi 710049, P. R. China*

Chen Zhao − *College of Chemistry, Jilin Province Research Center for Engineering and Technology of Spectral Analytical Instruments, Jilin University, Changchun 130012, P. R. China*

Xuran Dai − *College of Chemistry, Jilin Province Research Center for Engineering and Technology of Spectral Analytical Instruments, Jilin University, Changchun 130012, P. R. China*

Mo Ma − *College of Chemistry, Jilin Province Research Center for Engineering and Technology of Spectral Analytical Instruments, Jilin University, Changchun 130012, P. R. China*

Pinyi Ma − *College of Chemistry, Jilin Province Research Center for Engineering and Technology of Spectral Analytical Instruments, Jilin University, Changchun 130012, P. R. China;* orcid.org/0000-0002-3230-4928

Daqian Song − *College of Chemistry, Jilin Province Research Center for Engineering and Technology of Spectral Analytical Instruments, Jilin University, Changchun 130012, P. R. China;* orcid.org/0000-0002-4866-1292

Yongxi Zhao − *Institute of Analytical Chemistry and Instrument for Life Science, The Key Laboratory of Biomedical Information Engineering of Ministry of Education, School of Life Science and Technology, Xi'an Jiaotong University, Xi'an, Shaanxi 710049, P. R. China; Frontier Institute of Science and Technology, and Interdisciplinary Research Center of Frontier Science and Technology, Xi'an Jiaotong University, Xi'an, Shaanxi 710049, P. R. China;* orcid.org/0000-0002-1796-7651

Complete contact information is available at: https://pubs.acs.org/10.1021/jacsau.5c00870

Author Contributions

#These authors contributed equally.

Notes

The authors declare no competing financial interest.

ACKNOWLEDGMENTS

This work was supported by the National Natural Science Foundation of China (No. 22125404 and 92068118) and the Innovation Capability Support Program of Shaanxi (No. 2023-CX-TD-62).

REFERENCES

(1) Harris-Tryon, T. A.; Grice, E. A. Microbiota and maintenance of skin barrier function. *Science* **2022**, *376* (6596), 940−945.

(2) Paliwal, S.; Hwang, B. H.; Tsai, K. Y.; Mitragotri, S. Diagnostic opportunities based on skin biomarkers. *Eur. J. Pharm. Sci.* **2013**, *50* (5), 546−556.

(3) Friedel, M.; Thompson, I. A. P.; Kasting, G.; Polsky, R.; Cunningham, D.; Soh, H. T.; Heikenfeld, J. Opportunities and challenges in the diagnostic utility of dermal interstitial fluid. *Nat. Biomed. Eng.* **2023**, *7* (12), 1541−1555.

(4) Zhang, J.; Yu, H. Y.; Man, M. Q.; Hu, L. Z. Aging in the dermis: Fibroblast senescence and its significance. *Aging Cell* **2024**, *23* (2), No. e14054.

(5) Tracy, L. E.; Minasian, R. A.; Caterson, E. J. Extracellular Matrix and Dermal Fibroblast Function in the Healing Wound. *Adv. Wound Care* **2016**, *5* (3), 119−136.

(6) Capolupo, L.; Khven, I.; Lederer, A. R.; Mazzeo, L.; Glousker, G.; Ho, S.; Russo, F.; Montoya, J. P.; Bhandari, D. R.; Bowman, A. P.; et al. Sphingolipids control dermal fibroblast heterogeneity. *Science* **2022**, *376* (6590), No. eabh1623.

(7) Zada, M.; Pattamatta, U.; White, A. Modulation of Fibroblasts in Conjunctival Wound Healing. *Ophthalmology* **2018**, *125* (2), 179−192.

(8) Calabrese, E. J.; Dhawan, G.; Kapoor, R.; Agathokleous, E.; Calabrese, V. Hormesis: wound healing and fibroblasts. *Pharmacol. Res.* **2022**, *184*, No. 106449.

(9) Talbott, H. E.; Mascharak, S.; Griffin, M.; Wan, D. C.; Longaker, M. T. Wound healing, fibroblast heterogeneity, and fibrosis. *Cell Stem Cell* **2022**, *29* (8), 1161−1180.

(10) Yao, Y.; Zhang, A.; Yuan, C.; Chen, X.; Liu, Y. Recent trends on burn wound care: hydrogel dressings and scaffolds. *Biomater. Sci.* **2021**, *9* (13), 4523−4540.

(11) Huse, M. Mechanical forces in the immune system. *Nat. Rev. Immunol.* **2017**, *17* (11), 679−690.

(12) Villeneuve, C.; McCreery, K. P.; Wickström, S. A. Measuring and manipulating mechanical forces during development. *Nat. Cell Biol.* **2025**, *27* (4), 575−590.

(13) Sun, Z.; Costell, M.; Fässler, R. Integrin activation by talin, kindlin and mechanical forces. *Nat. Cell Biol.* **2019**, *21* (1), 25−31.

(14) Sutlive, J.; Xiu, H. N.; Chen, Y. F.; Gou, K.; Xiong, F. Z.; Guo, M.; Chen, Z. Generation, Transmission, and Regulation of Mechanical Forces in Embryonic Morphogenesis. *Small* **2022**, *18* (6), No. 2103466.

(15) Evans, E. A.; Calderwood, D. A. Forces and Bond Dynamics in Cell Adhesion. *Science* **2007**, *316* (5828), 1148−1153.

(16) Hoffman, B. D.; Grashoff, C.; Schwartz, M. A. Dynamic molecular processes mediate cellular mechanotransduction. *Nature* **2011**, *475* (7356), 316−323.

(17) Parsons, J. T.; Horwitz, A. R.; Schwartz, M. A. Cell adhesion: integrating cytoskeletal dynamics and cellular tension. *Nat. Rev. Mol. Cell Biol.* **2010**, *11* (9), 633−643.

(18) Harburger, D. S.; Calderwood, D. A. Integrin signalling at a glance. *J. Cell Sci.* **2009**, *122* (9), 1472.

(19) Qiu, Y.; Brown, A. C.; Myers, D. R.; Sakurai, Y.; Mannino, R. G.; Tran, R.; Ahn, B.; Hardy, E. T.; Kee, M. F.; Kumar, S.; et al. Platelet mechanosensing of substrate stiffness during clot formation mediates adhesion, spreading, and activation. *Proc. Natl. Acad. Sci. U.S.A.* **2014**, *111* (40), 14430−14435.

(20) Colin-York, H.; Eggeling, C.; Fritzsche, M. Dissection of mechanical force in living cells by super-resolved traction force microscopy. *Nat. Protoc.* **2017**, *12* (4), 783−796.

(21) Lee, M.; Jeong, H.; Lee, C.; Lee, M. J.; Delmo, B. R.; Heo, W. D.; Shin, J. H.; Park, Y. High-resolution assessment of multidimensional cellular mechanics using label-free refractive-index traction force microscopy. *Commun. Biol.* **2024**, *7* (1), No. 115.

(22) Siadat, S. M.; Ruberti, J. W. Mechanochemistry of collagen. *Acta Biomater.* **2023**, *163*, 50−62.

(23) Duan, M. M.; Xia, S.; Liu, Y.; Pu, X. H.; Chen, Y. K.; Zhou, Y. L.; Huang, M. L.; Pi, C. X.; Zhang, D. M.; Xie, J. Stiffened fibre-like microenvironment based on patterned equidistant micropillars directs chondrocyte hypertrophy. *Mater. Today Bio* **2023**, *20*, No. 100682.

(24) Zhang, Y.; Ge, C. H.; Zhu, C.; Salaita, K. DNA-based digital tension probes reveal integrin forces during early cell adhesion. *Nat. Commun.* **2014**, *5* (1), No. 5167.

(25) Wang, X.; Ha, T. Defining Single Molecular Forces Required to Activate Integrin and Notch Signaling. *Science* **2013**, *340* (6135), 991−994.

(26) Zhao, Y.; Pal, K.; Tu, Y.; Wang, X. Cellular Force Nanoscopy with 50 nm Resolution Based on Integrin Molecular Tension Imaging and Localization. *J. Am. Chem. Soc.* **2020**, *142* (15), 6930−6934.

(27) Kim, Y.; Kim, K. A.; Kim, B. C. Double-stranded DNA force sensors to study the molecular level forces required to activate signaling pathways. *J. Korean Phys. Soc.* **2021**, *78* (5), 386−392.

(28) Hu, Y.; Ma, V. P. Y.; Ma, R.; Chen, W.; Duan, Y.; Glazier, R.; Petrich, B. G.; Li, R.; Salaita, K. DNA-Based Microparticle Tension Sensors (μTS) for Measuring Cell Mechanics in Non-planar Geometries and for High-Throughput Quantification. *Angew. Chem., Int. Ed.* **2021**, *60* (33), 18044−18050.

(29) Vora, L. K.; Sabri, A. H.; McKenna, P. E.; Himawan, A.; Hutton, A. R. J.; Detamornrat, U.; Paredes, A. J.; Larrañeta, E.; Donnelly, R. F. Microneedle-based biosensing. *Nat. Rev. Bioeng.* **2024**, *2* (1), 64−81.

(30) Li, Z. Y.; Wang, Y. H.; Zhang, R. W.; Liu, Z. J.; Chang, Z. Y.; Deng, Y. L.; Qi, X. Y. Microneedles-Based Theranostic Platform: From the Past to the Future. *ACS Nano* **2024**, *18* (35), 23876−23893.

(31) Tehrani, F.; Teymourian, H.; Wuerstle, B.; Kavner, J.; Patel, R.; Furmidge, A.; Aghavali, R.; Hosseini-Toudeshki, H.; Brown, C.; Zhang, F.; et al. An integrated wearable microneedle array for the continuous monitoring of multiple biomarkers in interstitial fluid. *Nat. Biomed. Eng.* **2022**, *6* (11), 1214−1224.

(32) Wang, K.; Cai, L. J.; Fan, L.; Wang, L.; Bian, F. K.; Sun, W. J.; Zhao, Y. J. Electrical Microneedles for Wound Treatment. *Adv. Sci.* **2025**, *12* (24), No. 2409519.

(33) Mage, P. L.; Ferguson, B. S.; Maliniak, D.; Ploense, K. L.; Kippin, T. E.; Soh, H. T. Closed-loop control of circulating drug levels in live animals. *Nat. Biomed. Eng.* **2017**, *1* (5), No. 0070.

(34) Keyvani, F.; Ghavaminejad, P.; Saleh, M. A.; Soltani, M.; Zhao, Y. S.; Sadeghzadeh, S.; Shakeri, A.; Chelle, P.; Zheng, H. J.; Rahman, F. A.; et al. Integrated Electrochemical Aptamer Biosensing and

Colorimetric pH Monitoring via Hydrogel Microneedle Assays for Assessing Antibiotic Treatment. *Adv. Sci.* **2024**, *11* (41), No. 2309027.

(35) Mo, R.; Zhang, H.; Xu, Y.; Wu, X. Y.; Wang, S. Q.; Dong, Z.; Xia, Y. M.; Zheng, D. F.; Tan, Q. Transdermal drug delivery via microneedles to mediate wound microenvironment. *Adv. Drug Delivery Rev.* **2023**, *195*, No. 114753.

(36) Wu, Y.; Tehrani, F.; Teymourian, H.; Mack, J.; Shaver, A.; Reynoso, M.; Kavner, J.; Huang, N.; Furmidge, A.; Duvvuri, A.; et al. Microneedle Aptamer-Based Sensors for Continuous, Real-Time Therapeutic Drug Monitoring. *Anal. Chem.* **2022**, *94* (23), 8335−8345.

(37) Dong, J.; Wen, L.; Yang, H.; Zhao, J.; He, C.; Hu, Z.; Peng, L.; Hou, C.; Huo, D. Catalytic Hairpin Assembly-Driven Ratiometric Dual-Signal Electrochemical Biosensor for Ultrasensitive Detection of MicroRNA Based on the Ratios of Fe-MOFs and MB-GA-UiO-66-NH2. *Anal. Chem.* **2022**, *94* (15), 5846−5855.

(38) Zhang, Q.; Fu, Y.; Xiao, K.; Du, C.; Zhang, X.; Chen, J. Sensitive Dual-Mode Biosensors for CYFRA21−1 Assay Based on the Dual-Signaling Electrochemical Ratiometric Strategy and "On−Off−On" PEC Method. *Anal. Chem.* **2021**, *93* (17), 6801−6807.

(39) Love, J. C.; Estroff, L. A.; Kriebel, J. K.; Nuzzo, R. G.; Whitesides, G. M. Self-Assembled Monolayers of Thiolates on Metals as a Form of Nanotechnology. *Chem. Rev.* **2005**, *105* (4), 1103−1170.

(40) Arroyo-Currás, N.; Scida, K.; Ploense, K. L.; Kippin, T. E.; Plaxco, K. W. High Surface Area Electrodes Generated via Electrochemical Roughening Improve the Signaling of Electrochemical Aptamer-Based Biosensors. *Anal. Chem.* **2017**, *89* (22), 12185−12191.

(41) Zakaria, N. D.; Omar, M. H.; Kamal, N. N. A.; Razak, K. A.; Sönmez, T.; Balakrishnan, V.; Hamzah, H. H. Effect of Supporting Background Electrolytes on the Nanostructure Morphologies and Electrochemical Behaviors of Electrodeposited Gold Nanoparticles on Glassy Carbon Electrode Surfaces. *ACS Omega* **2021**, *6* (38), 24419−24431.

(42) Gupta, N. K.; Wilkinson, E. A.; Karuppannan, S. K.; Bailey, L.; Vilan, A.; Zhang, Z.; Qi, D.-C.; Tadich, A.; Tuite, E. M.; Pike, A. R.; et al. Role of Order in the Mechanism of Charge Transport across Single-Stranded and Double-Stranded DNA Monolayers in Tunnel Junctions. *J. Am. Chem. Soc.* **2021**, *143* (48), 20309−20319.

(43) Kékedy-Nagy, L.; Shipovskov, S.; Ferapontova, E. E. Effect of a Dual Charge on the DNA-Conjugated Redox Probe on DNA Sensing by Short Hairpin Beacons Tethered to Gold Electrodes. *Anal. Chem.* **2016**, *88* (16), 7984−7990.

(44) Li, H.; Dauphin-Ducharme, P.; Ortega, G.; Plaxco, K. W. Calibration-Free Electrochemical Biosensors Supporting Accurate Molecular Measurements Directly in Undiluted Whole Blood. *J. Am. Chem. Soc.* **2017**, *139* (32), 11207−11213.

(45) Li, C.; Lu, J.; Feng, Y.; Guo, Y.; Wang, J.; Song, Y.; Li, R.; Tian, L. Signal amplification strategy electrochemiluminescence based on porous graphite-phase carbon nitride: A novel ECL sensor for ultrasensitive detection of tigecycline. *Carbon* **2025**, *233*, No. 119857.

(46) Chen, Y.; Yang, H.; Feng, H.; Yang, P.; Zhang, J.; Shu, B. Electrodeposition and corrosion performance of Ni-Co alloys with different cobalt contents. *Mater. Today Commun.* **2023**, *35*, No. 106058.

(47) Zhang, H.; Pan, Y.; Hou, Y.; Li, M.; Deng, J.; Wang, B.; Hao, S. Smart Physical-Based Transdermal Drug Delivery System:Towards Intelligence and Controlled Release. *Small* **2024**, *20* (9), No. 2306944.

(48) Zheng, M.; Sheng, T.; Yu, J.; Gu, Z.; Xu, C. Microneedle biomedical devices. *Nat. Rev. Bioeng.* **2024**, *2* (4), 324−342.

(49) Connor, E. E.; Mwamuka, J.; Gole, A.; Murphy, C. J.; Wyatt, M. D. Gold Nanoparticles Are Taken Up by Human Cells but Do Not Cause Acute Cytotoxicity. *Small* **2005**, *1* (3), 325−327.

(50) Zheng, B.; Li, Q. Y.; Fang, L. P.; Cai, X. L.; Liu, Y.; Duo, Y.; Li, B. W.; Wu, Z. Y.; Shen, B. X.; Bai, Y.; et al. Microorganism microneedle micro-engine depth drug delivery. *Nat. Commun.* **2024**, *15* (1), No. 8947.

(51) Makvandi, P.; Kirkby, M.; Hutton, A. R. J.; Shabani, M.; Yiu, C. K. Y.; Baghbantaraghdari, Z.; Jamaledin, R.; Carlotti, M.; Mazzolai, B.; Mattoli, V.; Donnelly, R. F. Engineering Microneedle Patches for Improved Penetration: Analysis, Skin Models and Factors Affecting Needle Insertion. *Nano-Micro Lett.* **2021**, *13* (1), No. 93.